Rapid Communications

Ultrafast electron dynamics reveal the high potential of InSe for hot-carrier optoelectronics

Zhesheng Chen,[1] Christine Giorgetti,[1] Jelena Sjakste,[1] Raphael Cabouat,[1] Valérie Véniard,[1] Zailan Zhang,[2] Amina Taleb-Ibrahimi,[3] Evangelos Papalazarou,[4] Marino Marsi,[4] Abhay Shukla,[2] Jacques Peretti,[5] and Luca Perfetti[1]

[1]*Laboratoire des Solides Irradiés, Ecole Polytechnique, CNRS, CEA, Université Paris-Saclay, 91128 Palaiseau Cedex, France*

[2]*Institut de Minéralogie, de Physique des Matériaux et de Cosmochimie, Sorbonne Universités - UPMC Université Paris 06, CNRS-UMR7590, 4 Place Jussieu, 75252 Paris, France*

[3]*Société Civile Synchrotron SOLEIL, L'Orme des Merisiers, Saint-Aubin, BP 48, 91192 Gif-sur-Yvette, France*

[4]*Laboratoire de Physique des Solides, CNRS, Université Paris-Sud, Université Paris-Saclay, 91405 Orsay, France*

[5]*Laboratoire de Physique de la Matière Condensée, Ecole Polytechnique, CNRS, CEA, Université Paris-Saclay, 91128 Palaiseau Cedex, France*

(Received 17 March 2018; published 4 June 2018)

We monitor the dynamics of hot carriers in InSe by means of two-photon photoelectron spectroscopy (2PPE). The electrons excited by photons of 3.12 eV experience a manifold relaxation. First, they thermalize to electronic states degenerate with the $\bar{M}$ valley. Subsequently, the electronic cooling is dictated by Fröhlich coupling with phonons of small momentum transfer. *Ab initio* calculations predict cooling rates that are in good agreement with the observed dynamics. We argue that electrons accumulating in states degenerate with the $\bar{M}$ valley could travel through a multilayer flake of InSe with a lateral size of 1 μm. The hot carriers pave a viable route to the realization of below-band-gap photodiodes and Gunn oscillators. Our results indicate that these technologies may find a natural implementation in future devices based on layered chalcogenides.

DOI: 10.1103/PhysRevB.97.241201

The van der Waals chalcogenides display a variety of different specifics that depend on their composition and number of layers. Weak mechanical binding of atoms along the stacking direction facilitates the realization of heterostructures with different functionalities. Some recent achievements have been the fine tuning of the band gap [1–3], the control of valley polarization [4], and the realization of devices with high mobility [5–7]. In this context, InSe is one of the building blocks with the highest potentials.

The bulk crystals of InSe can be thinned down to a few layers and encapsulated in hexagonal boron nitride (hBN) [7]. By these means, Bandurin and collaborators have fabricated transistors whose quality is high enough to observe Shubnikov–de Haas oscillations and the quantum Hall effect [7]. These results point out the two aspects making InSe particularly appealing. On one hand, the mobility of charge carriers rivals the one measured in graphene [8,9]. On the other hand, the bulk band gap of 1.26 eV is ideally suited for optoelectronic devices. Indeed, several groups have recently reported that InSe [10,11] and graphene/InSe heterostructures [12] have excellent photoresponsivity in the visible spectral region. Such photodetectors could be patterned on a large scale over flexible supports [13]. Eventually, the application of a larger bias can drive the photodetector in the avalanche regime [14].

The conception of devices based on InSe would greatly profit from a precise knowledge of the transient state following photoexcitation. Some pioneering experiments have investigated the coherent propagation and dephasing of the exciton-polariton [15,16]. These optical methods revealed a beating polarization induced by resonant pulses, but provided no insights on the energy relaxation of hot carriers. Here, we address this issue by mapping the dynamics of excited electrons in reciprocal space [17,18]. Our two-photon photoemission (2PPE) data show that photoexcitation above the $\bar{M}$ valley results in a high density of electrons with an excess energy of $\cong$0.6 eV and a cooling time of 2 ps. First-principles calculations of electron-phonon coupling discriminate between the distinct scattering mechanisms during the cooling process. The relevance of such hot carriers for the design of tunable photodetectors and Gunn oscillators is briefly discussed.

Single crystals of ε-InSe have been grown using the Bridgmann method from a nonstoichiometric melt [19]. The crystallographic structure of ε-InSe is displayed in Fig. 1(a) (top and side views, respectively, left and right). Ultraviolet photoemission and photoluminescence spectra show that our bulk crystal is naturally n doped and has a direct band gap of 1.26 eV. We plot in Fig. 1(b) the calculated bulk band structure projected on the surface plane, along the $\bar{\Gamma}$-$\bar{M}$ of the hexagonal Brillouin zone (BZ) (see inset). The red dashed and orange dotted lines point out the extension of the projected first conduction band. The correspondence between the bulk and surface BZ, a band structure along the complete $\bar{\Gamma}$-$\bar{K}$-$\bar{M}$-$\bar{\Gamma}$ path for a larger energy range, as well as the technical details of the *ab initio* calculations, are given in the Supplemental Material [20]. We plot in Fig. 1(c) the electronic density of states (DOS) calculated by density functional theory (DFT), using the ABINIT code [21], with lattice parameters from Ref. [22] (see Supplemental Material [20]). As show by Fig. 1(c), the density of electronic states in the conduction band abruptly increases when the excess energy overcomes the bottom of the $\bar{M}$ valley.

Our photon source is a Ti:sapphire laser system delivering 6 μJ pulses with a repetition rate of 250 kHz. Part of the fundamental beam ($\omega = 1.56$ eV) is converted to the second harmonic ($2\omega = 3.12$ eV) in a β-BaB_2O_4 (BBO)

 ©2018 American Physical Society

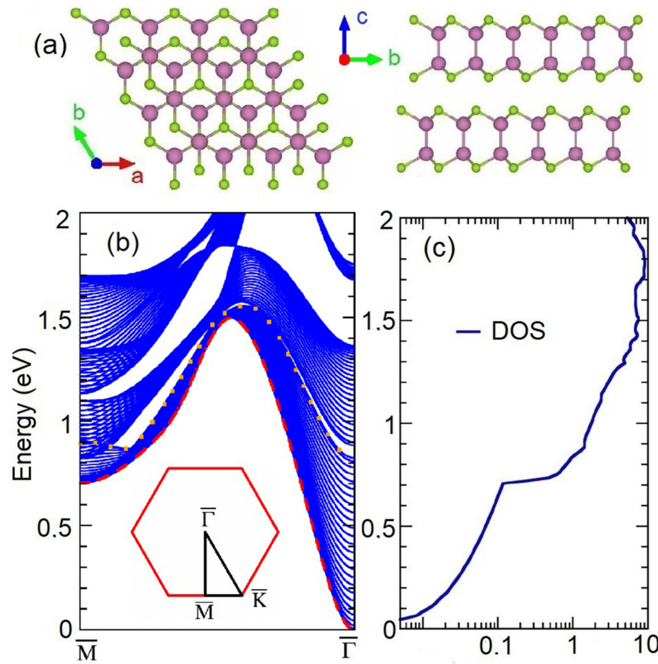

FIG. 1. (a) Crystal structure of ε-InSe. (b) Projected band structure along the high-symmetry direction $\bar{\Gamma}$-$\bar{M}$. The projected states of the first conduction band span the area between the red dashed line and the orange dotted line. The inset displays the surface Brillouin zone. (c) Electronic DOS as a function of excess energy, in units of electron/cell/eV.

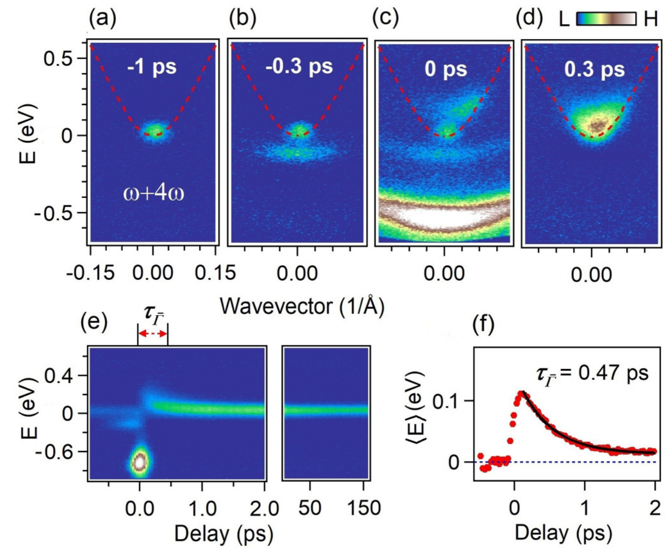

FIG. 2. The 2PPE data of this figure is generated by $\omega = 1.56$ eV and $4\omega = 6.24$ eV photons. (a)–(d) Photoelectron intensity maps acquired along the $\bar{\Gamma}$-$\bar{M}$ direction and plotted as a function of excess energy for different delay times. The red dashed line is the conduction band dispersion. (e) Dynamics of photoelectron intensity integrated in the wave-vector interval $[-0.1,0.1]$ Å^{-1}. (f) Average excess energy of the electrons in the conduction band as a function of pump-probe delay. The solid line is an exponential fit with decay time $\tau_{\bar{\Gamma}} = 0.47$ ps.

crystal while the rest is employed to generate the third harmonic ($3\omega = 4.68$ eV) and fourth harmonic beam ($4\omega = 6.24$ eV) [23]. We photoexcite the sample either by the ω or 2ω pulses, generating carriers density of 8×10^{17} cm^{-3} and 7×10^{18} cm^{-3}, respectively. The electrons emitted by the 3ω or 4ω pulse are discriminated in kinetic energy and angle with a resolution of 50 meV and 0.5°, respectively. Independently on the configuration of the experiment, the two beams generating the 2PPE signal display a cross correlation with a full width at half maximum FWHM < 0.16 ps. All samples have been cleaved at a base pressure of 8×10^{-11} mbar and measured at a temperature of 125 K.

Figures 2(a)–2(d) shows the photoelectron intensity maps acquired along the $\bar{\Gamma}$-$\bar{M}$ direction at different delay times t between the ω pulse and 4ω pulse. The image collected 1 ps before the arrival of the ω beam [Fig. 2(a)] is representative of the system in equilibrium conditions. According to the nominal n doping, we observe electrons in the conduction band minimum at an excess energy $E = E_{\bar{\Gamma}} = 0$ eV. Two image-potential states below $E_{\bar{\Gamma}}$ are excited by the 4ω beam and are detected, at negative t, by the ω pulse [Figs. 2(b) and 2(c)]. Due to the short lifetime, the lowest image-potential state is clearly visible only in the intensity map of Fig. 2(c). This map has been acquired at a nominal value of zero delay and can be viewed as a snapshot of the primary excitations. We remark yet in Fig. 2(c) that the ω pulse populates the conduction band up to $E = \omega - \Delta = 0.25$ eV where Δ is the band gap of InSe. The internal thermalization of such hot carriers proceeds faster than the cooling, probably because of an additional contribution of electron-electron scattering.

Figure 2(e) shows the photoelectron intensity $I(E,t)$ integrated in the wave-vector window $[-0.1,0.1]$ Å^{-1} and plotted as a function of pump-probe delay. The average excess energy $\langle E\rangle$ of the electrons in the conduction band is obtained by evaluating the integral $\int EI(E,t)dE/\int I(E,t)dE$ in the interval $E \in [0,0.5]$ eV. As shown by Fig. 2(f), the $\langle E\rangle$ has an initial value of $\langle E\rangle_0 = 0.12$ eV and it follows an exponential decay with time constant $\tau_{\bar{\Gamma}} = 0.47 \pm 0.2$ ps. This timescale elucidates the main relaxation mechanism of hot carriers in the $\bar{\Gamma}$ valley. We recall that a long-range Fröhlich interaction diverges in a material with three-dimensional periodicity. Therefore, the polar optical coupling becomes the dominant electron-phonon scattering channel for small momentum transfer [24,25].

Our calculations of vibrational properties and deformation potentials [26–28] (see Supplemental Material [20]) confirm the important role of polar interactions in intravalley cooling. We estimate the energy dissipation rate $\lambda = d\langle E\rangle/dt$ between 0.21 and 0.24 eV/ps at 125 K. Due to the long-range nature of the Fröhlich coupling, the phonon emission is weakly sensitive to the variation of the electronic DOS. Therefore, λ is almost independent on $\langle E\rangle$ as long as the excess energy is sufficiently larger than the phonon frequency. According to our theoretical estimate, hot carriers with an initial value $\langle E\rangle_0 = 0.12$ eV require a characteristic time $\langle E\rangle_0/\lambda = 0.57$ ps to approach the asymptotic level. The reasonably good agreement between $\langle E\rangle_0/\lambda$ and the experimental $\tau_{\bar{\Gamma}}$ confirms that our simple analysis provides an accurate description of the observed cooling.

Next, we investigate the photoexcited state generated by pumping and probing the sample with 2ω and 4ω pulses, respectively. We mark in Fig. 3(a) the three indicative areas

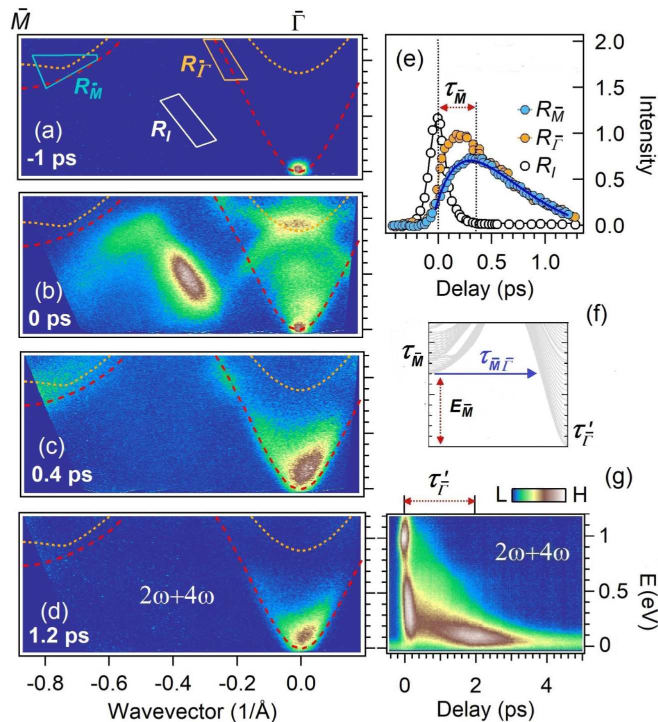

FIG. 3. The 2PPE data of this figure are generated by $2\omega = 3.12$ eV and $4\omega = 6.24$ eV photons. (a)–(d) Photoelectron intensity maps acquired along the $\bar{\Gamma}$-$\bar{M}$ direction, and plotted as a function of excess energy for different delay times. The projected states of the conduction band span the area between the red dashed line and the orange dotted line. (e) Dynamics of photoelectron intensity in the $\bar{M}$ valley ($R_{\bar{M}}$), in the virtual intermediate state (R_I), and in the $\bar{\Gamma}$ valley ($R_{\bar{\Gamma}}$). The explicit integration areas of the photoemission signal are indicated in the upper panel of (a). (f) Sketch of the projected band structure with characteristic timescales of $\bar{M}$ valley, $\bar{\Gamma}$ valley thermalization, and intervalley scattering. (g) Dynamics of photoelectron intensity integrated in the wave-vector interval $[-0.25,0.25]$ Å^{-1}.

$R_{\bar{M}}$, $R_{\bar{\Gamma}}$, and R_I on the 2PPE intensity map. As shown in Fig. 3(b), the absorption of 2ω photons results in a rich variety of spectral features. The projected states of the conduction band span between the red dashed line and the orange dotted line that are superimposed on the intensity maps. This guideline is useful to discriminate between different processes leading to photoemitted electrons. On one hand, the strong and dispersing signal that is located in the projected band gap is due to direct 2PPE emission via virtual states (very strong in R_I). Such photoelectrons may mimic the initial state dispersion and become intense when propagating in emitted waves that match the boundary conditions. On the other hand, real intermediate states of the $\bar{\Gamma}$ valley are excited by direct optical transitions from the p_x, p_y orbitals of the valence band. As in the case of GaAs, efficient intervalley scattering can rapidly randomize the wave vector of electrons with high excess energy [25,29]. This process sets in when E overcomes the bottom of the $\bar{M}$ valley at $E_{\bar{M}} = 0.7$ eV. By comparing Fig. 3(b) with Fig. 3(c), we deduce that electrons have already reached $E_{\bar{M}}$ at $t = 0.4$ ps (see the evolution of the signal in $R_{\bar{M}}$). Furthermore, intervalley scattering steadily refills the states of the $\bar{\Gamma}$ valley that are degenerate with $E_{\bar{M}}$ (signal in $R_{\bar{\Gamma}}$).

The dynamics of excited electrons can be tracked by focusing on selected regions in reciprocal space. We have integrated the 2PPE signal in the three indicative areas $R_{\bar{M}}$, $R_{\bar{\Gamma}}$, and R_I of Fig. 3(a). As shown by Fig. 3(e), the photoemission assisted by virtual states (R_I) follows the cross correlation between the pump and probe pulse. This signal has been employed to estimate the duration of optical pulses and to precisely determine zero delay. Note that states at the bottom of the $\bar{M}$ valley ($R_{\bar{M}}$) reach the highest occupation for $\tau_{\bar{M}} = 0.36$ ps. Although these electrons lose initial momentum within a few tens of femtoseconds, their energy dissipation is restrained by the low quantum energy of the emitted phonons. The most relevant modes that are involved in the scattering process are acoustic branches close to the zone boundary and with a typical energy of $\Omega \cong 14$ meV. Our calculations indicate that electrons with $E - E_{\bar{M}} \cong 0.5$ eV scatter with such phonons on an average timescale of 8 fs at 125 K. The energy dissipation time at high excess energies is mostly determined by short-wavelength phonon scattering, which depends strongly on the excess energy. According to our theoretical estimates the electrons that are at 0.5 eV above $E_{\bar{M}}$ require a characteristic time constant of 0.2 ps to reach the bottom of the $\bar{M}$ valley (see Supplemental Material [20]).

Figure 3(e) shows also that $R_{\bar{M}}$ electrons in the $\bar{M}$ valley and $R_{\bar{\Gamma}}$ electrons in the $\bar{\Gamma}$ valley display an identical dynamics for $t > \tau_{\bar{M}}$. These nearly degenerate states are maintained in detailed balance conditions by phonons with a wave vector near to the $\bar{M}$ point. The transition time calculated at 125 K is $\tau_{\bar{M}\to\bar{\Gamma}} = 180$ fs and it turns out to be short enough to confirm our conjecture. Eventually, the large $E_{\bar{M}} = 0.7$ eV may suggest that 180 fs (or 80 fs at 300 K) is surprisingly long. This result is not derived from unconventional matrix elements of electron-phonon coupling but rather from the small DOS of the $\bar{\Gamma}$ valley at $E_{\bar{M}}$ [see Fig. 1(c)]. We find a comparison of InSe with other chalcogenides to be instructive: Electrons that are resonantly excited at 300 K in the $\bar{M}$ valley of bulk MoS_2 [30] or WSe_2 [31] require $\tau_{\bar{M}\to\bar{\Sigma}} < 80$ fs to reach the $\bar{\Sigma}$ valley and the energy separation between $\bar{M}$ and $\bar{\Sigma}$ valley is only $E_{\bar{M}} - E_{\bar{\Sigma}} = 0.2$ eV. In the case of InSe, the excess energy is particularly large and therefore the carriers can be sustained above the conduction band minimum for a long time. Moreover, an abrupt increase of the DOS for $E > E_{\bar{M}} = 0.7$ eV can boost the injection of electrons in the $\bar{M}$ valley. Once these electrons fall below $E_{\bar{M}}$, the intervalley scattering is no longer active whereas the cooling proceeds mainly via Fröling coupling to phonons with a small momentum transfer [25,29]. Figure 3(g) shows the photoelectron signal integrated around the $\bar{\Gamma}$ valley in a wave-vector window of $[-0.25,0.25]$ Å^{-1}. The maximal carrier density at the bottom of the conduction band is achieved $\tau_{\bar{\Gamma}'} = 2$ ps after photoexcitation.

Figures 4(a) and 4(b) display the 2PPE signal probed in the $\bar{\Gamma}$ valley by 3ω photons and excited with 2ω and ω, respectively. Being independent on the DOS, the Fröhlich dissipation rate is the same in both cases. However, the electrons hailing from the $\bar{M}$ valley gather in the $\bar{\Gamma}$ valley near the calculated $E_{\bar{M}}$. As a consequence, energy dissipation takes much longer in Fig. 4(a) than in Fig. 4(b). By assuming that intervalley scattering generates an average kinetic energy $\langle E \rangle \cong 0.4$–$0.6$ eV, the

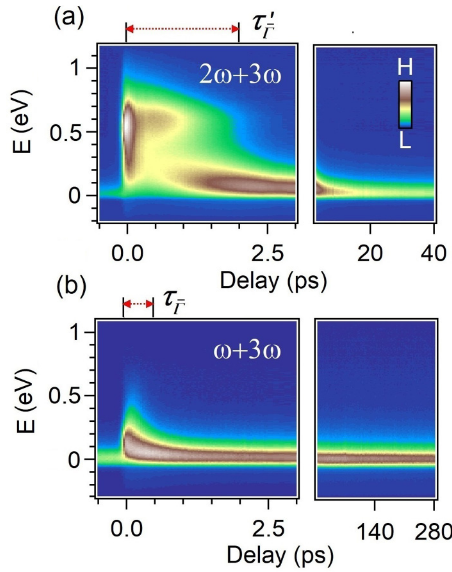

FIG. 4. The 2PPE data of this figure have been collected by probing photoelectrons with $3\omega = 4.68$ eV photons. Dynamics of electrons excited in the $\bar{\Gamma}$ valley by photons of (a) $2\omega = 3.12$ eV and (b) $\omega = 1.56$ eV. Long-living hot carriers take place only upon photoexcitation with 2ω pulses.

resulting cooling time $\langle E\rangle/\lambda = 1.6$–$2.5$ ps is consistent with the observed $\tau_{\bar{\Gamma}'}$.

Next, we estimate the minimal distance d at which two electrodes should be placed in order to extract the hot carriers. The effective mobility $\mu = 600\ \text{cm}^2\ \text{V}^{-1}\ \text{s}^{-1}$ is given by the model for linear dispersion [32] at 0.7 eV excess energy and 125 K (see Supplemental Material [20]). Due to the high excess energy of hot electrons, the nominal μ is lower than the mobility measured in InSe transistors [7]. Nonetheless, a driven drift can still attain high values. Upon an applied voltage of $V = 10$ V, the hot electrons reach the electrodes if $d = \sqrt{V\mu\tau'_{\bar{\Gamma}}} \cong 1\ \mu\text{m}$.

The relatively large distance that can be covered by hot carriers suggests original concepts for optoelectronic applications. Recently, Lao *et al.* developed a long-wavelength photodetection principle working with far from equilibrium conditions [33]. Hot carriers injected into a p-doped GaAs structure interact with cold carriers and promote them to states of high excess energy. The tunneling of such holes through $\text{Al}_x\text{Ga}_{1-x}\text{As}$ barriers enables a long-wavelength infrared response that can be tuned via the applied voltage. By direct analogy, the hot electrons in the $\bar{M}$ valley of InSe could extend such a promising approach to chalcogenide heterostructures.

A second possible application of hot-carrier generation are Gunn diodes. In III/V semiconductors, a microwave signal of high frequency appears if the applied bias field exceeds a threshold value [34]. This effect arises when the high electrical field promotes electrons from the conduction band minimum to an upper valley [34,35]. As a consequence, the average mobility of electrons decreases, while the device enters in a regime of negative differential resistance. The heavy mass of the $\bar{M}$ valley should favor this process also in InSe. If confirmed, our conjecture may lead to the development of microwave oscillators and bistable switches based on chalcogenide materials.

In conclusion, we have shown that InSe has an excellent potential for hot-carrier optoelectronics. The high-energy density of electronic states above the bottom of the $\bar{M}$ valley favors the photoassisted or electrical injection of electrons with a high excess energy. On the other hand, electrons that reached the $\bar{\Gamma}$ valley can dissipate energy only via Fröhlich coupling to optical phonons. These hot carriers have a typical lifetime of 2 ps and could be extracted from a device of $\sim 1\ \mu\text{m}$. We could successfully model the observed dynamics by first-principles calculations of the electron-phonon scattering. Our results will be of guidance for the physics of electron-phonon coupling in other layered chalcogenides. Moreover, we suggest appealing concepts, such as below-band-gap photodetection or a negative differential resistance, that could be shortly integrated into the family of van der Waals semiconductors.

We thank DIM-Oximore and the Ecole Polytechnique for funding under the project "ECOGAN." This work was supported by LABEX PALM (ANR-10-LABX-0039-PALM, Project Femtonic) and by the EU/FP7 under the contract Go Fast (Grant No. 280555). Computer time has been granted by GENCI (Project No. 2210) and by Ecole Polytechnique through the LLR-LSI project.

[1] K. F. Mak, C. Lee, J. Hone, J. Shan, and T. F. Heinz, Phys. Rev. Lett. **105**, 136805 (2010).
[2] V. Tran, R. Soklaski, Y. Liang, and L. Yang, Phys. Rev. B **89**, 235319 (2014).
[3] G. W. Mudd, S. A. Svatek, T. Ren, A. Patané, O. Makarovsky, L. Eaves, P. H. Beton, Z. D. Kovalyuk, G. V. Lashkarev, Z. R. Kudrynskyi, and A. I. Dmitriev, Adv. Mater. **25**, 5714 (2013).
[4] K. F. Mak, K. He, J. Shan, and T. F. Heinz, Nat. Nanotechnol. **7**, 494 (2012).
[5] B. Radisavljevic, A. Radenovic, J. Brivio, V. Giacometti, and A. Kis, Nat. Nanotechnol. **6**, 147 (2011).
[6] L. Li, Y. Yu, G. J. Ye, Q. Ge, X. Ou, H. Wu, D. Feng, X. H. Chen, and Y. Zhang, Nat. Nanotechnol. **9**, 372 (2014).
[7] D. A. Bandurin, A. V. Tyurnina, G. L. Yu, A. Mishchenko, V. Zólyomi, S. V. Morozov, R. K. Kumar, R. V. Gorbachev, Z. R. Kudrynskyi, S. Pezzini, Z. D. Kovalyuk, U. Zeitler, K. S. Novoselov, A. Patanè, L. Eaves, I. V. Grigorieva, V. I. Fal'ko, A. K. Geim, and Y. Cao, Nat. Nanotechnol. **12**, 223 (2017).
[8] K. I. Bolotin, K. J. Sikes, Z. Jiang, M. Klima, G. Fudenberg, J. Hone, P. Kim, and H. L. Stormera, Solid State Commun. **146**, 351 (2008).
[9] C. R. Dean, A. F. Young, I. Meric, C. Lee, L. Wang, S. Sorgenfrei, K. Watanabe, T. Taniguchi, P. Kim, K. L. Shepard, and J. Hone, Nat. Nanotechnol. **5**, 722 (2010).
[10] S. Lei, L. Ge, S. Najmaei, A. George, R. Kappera, J. Lou, M. Chhowalla, H. Yamaguchi, G. Gupta, R. Vajtai,

A. D. Mohite, and P. M. Ajayan, ACS Nano **8**, 1263 (2014).

[11] S. R. Tamalampudi, Y.-Y. Lu, R. U. Kumar, R. Sankar, C.-D. Liao, K. B. Moorthy, C.-H. Cheng, F. C. Chou, and Y.-T. Chen, Nano Lett. **14**, 2800 (2014).

[12] Z. Chen, J. Biscarasa, and A. Shukla, Nanoscale **7**, 5981 (2015).

[13] W. Zheng, T. Xie, Y. Zhou, Y. L. Chen, W. Jiang, S. Zhao, J. Wu, Y. Jing, Y. Wu, G. Chen, Y. Guo, J. Yin, S. Huang, H. Q. Xu, Z. Liu, and H. Peng, Nat. Commun. **6**, 6972 (2015).

[14] S. Lei, F. Wen, L. Ge, S. Najmaei, A. George, Y. Gong, W. Gao, Z. Jin, B. Li, J. Lou, J. Kono, R. Vajtai, P. Ajayan, and N. J. Halas, Nano Lett. **15**, 3048 (2015).

[15] S. Nüsse, P. H. Bolivar, H. Kurz, F. Levy, A. Chevy, and O. Lang, Phys. Rev. B **55**, 4620 (1997).

[16] P. Dey, J. Paul, N. Glikin, Z. D. Kovalyuk, Z. R. Kudrynskyi, A. H. Romero, and D. Karaiskaj, Phys. Rev. B **89**, 125128 (2014).

[17] Y. Ohtsubo, J. Mauchain, J. Faure, E. Papalazarou, M. Marsi, P. Le Fèvre, F. Bertran, A. Taleb-Ibrahimi, and L. Perfetti, Phys. Rev. Lett. **109**, 226404 (2012).

[18] A. G. Čabo, J. A. Miwa, S. S. Grønborg, J. M. Riley, J. C. Johannsen, C. Cacho, O. Alexander, R. T. Chapman, E. Springate, M. Grioni, J. V. Lauritsen, P. D. C. King, P. Hofmann, and S. Ulstrup, Nano Lett. **15**, 5883 (2015).

[19] A. Chevy, J. Cryst. Growth **67**, 119 (1984).

[20] See Supplemental Material at http://link.aps.org/supplemental/10.1103/PhysRevB.97.241201 for details on the theoretical calculations.

[21] X. Gonze, B. Amadon, P.-M. Anglade, J.-M. Beuken, F. Bottin, P. Boulanger, F. Bruneval, D. Caliste, R. Caracas, M. Côté *et al.*, Comput. Phys. Commun. **180**, 2582 (2009).

[22] S. J. Magorrian, V. Zòlyomi, and V. I. Fal'ko, Phys. Rev. B **94**, 245431 (2016).

[23] J. Faure, J. Mauchain, E. Papalazarou, W. Yan, J. Pinon, M. Marsi, and L. Perfetti, Rev. Sci. Instrum. **83**, 043109 (2012).

[24] J. Sjakste, N. Vast, M. Calandra, and F. Mauri, Phys. Rev. B **92**, 054307 (2015).

[25] H. Tanimura, J. Kanasaki, K. Tanimura, J. Sjakste, N. Vast, M. Calandra, and F. Mauri, Phys. Rev. B **93**, 161203(R) (2016).

[26] P. Giannozzi, O. Andreussi, T. Brumme, O. Bunau, M. B. Nardelli, M. Calandra, R. Car, C. Cavazzoni, D. Ceresoli, M. Cococcioni *et al.*, J. Phys.: Condens. Matter **29**, 465901 (2017); http://www.quantum-espresso.org.

[27] J. Sjakste, N. Vast, and V. Tyuterev, Phys. Rev. Lett. **99**, 236405 (2007).

[28] V. G. Tyuterev, S. V. Obukhov, N. Vast, and J. Sjakste, Phys. Rev. B **84**, 035201 (2011).

[29] J. Kanasaki, H. Tanimura, and K. Tanimura, Phys. Rev. Lett. **113**, 237401 (2014).

[30] R. Wallauer, J. Reimann, N. Armbrust, J. Güdde, and U. Höfer, Appl. Phys. Lett. **109**, 162102 (2016).

[31] R. Bertoni, C. W. Nicholson, L. Waldecker, H. Hübener, C. Monney, U. De Giovannini, M. Puppin, M. Hoesch, E. Springate, R. T. Chapman, C. Cacho, M. Wolf, A. Rubio, and R. Ernstorfer, Phys. Rev. Lett. **117**, 277201 (2016).

[32] W. Zhu, V. Perebeinos, M. Freitag, and P. Avouris, Phys. Rev. B **80**, 235402 (2009).

[33] Y. F. Lao, A. G. U. Perera, L. H. Li, S. P. Khanna, E. H. Linfield, and H. C. Liu, Nat. Photonics **8**, 412 (2014).

[34] P. N. Butcher, Rep. Prog. Phys. **30**, 97 (1967).

[35] D. E. McCumber and A. G. Chynoweth, IEEE Trans. Electron Devices **13**, 4 (1966).